



# Investigation on $Y_2NiMnO_6$ nanostructures for energy storage applications

T. Sharmili<sup>1</sup> · A. Joana Preethi<sup>1</sup> · J. Vigneshwaran<sup>2</sup> · Sujin P. Jose<sup>2</sup> · M. Ragam<sup>1</sup>

Received: 30 June 2022 / Accepted: 9 December 2022 / Published online: 20 December 2022  
© The Author(s), under exclusive licence to Springer-Verlag GmbH, DE part of Springer Nature 2022

## Abstract

In this present work, the double perovskite  $Y_2NiMnO_6$  nanostructures had been successfully synthesized through the hydrothermal route. Using various characterization techniques, the structural, morphological, impedance, dielectric, electrochemical, and magnetic properties were analyzed. The monoclinic ( $P2_1/n$ ) structure of the prepared  $Y_2NiMnO_6$  was confirmed using powder X-ray diffraction. Results from the scanning electron microscope showed the formation of  $Y_2NiMnO_6$  nanostructures. TEM image of  $Y_2NiMnO_6$  nanoparticles revealed d-spacing of 0.56 nm and selected area electron diffraction pattern showed (311) plane for  $Y_2NiMnO_6$ . Fast Fourier transform (FFT) analysis was performed on the lattice fringes and the diffraction spots indexed to the cubic spinel. The dielectric, impedance, modulus, and AC conductivity of the synthesized double perovskite  $Y_2NiMnO_6$  were studied in the frequency range of 100 Hz–5 MHz at room temperature. The effect of grain and grain boundary was analyzed by the Nyquist plot. The presence of non-Debye type of relaxation was confirmed from the dielectric, impedance, and modulus studies. The elaborated studies of complex impedance spectra provided the basis to understand the electrical properties, which had strong relations with the microstructure and resistive nature of the prepared material. The electrochemical behavior of the prepared  $Y_2NiMnO_6$  with three-electrode system was found to have pseudocapacitive nature with the specific capacitance value 8.633 F/g for 0.5 M KOH, 75.476 F/g for 1 M KOH, and 78.201 F/g for 2 M KOH at the scan rate of 10 mV/s. The specific capacitance values were improved by increasing the concentration of electrolyte. The vibration sample magnetometer of the synthesized  $Y_2NiMnO_6$  shows the paramagnetic behavior at room temperature.

**Keywords** Double perovskite · Monoclinic  $P2_1/n$  · Non-Debye relaxation · Pseudocapacitive · Paramagnetic

## 1 Introduction

In recent years, eco-friendly and clean energy have gained worldwide attention due to the increasing concerns about global warming and other environmental issues associated with the consumption of fossil fuels. Presently, new functional materials are extensively investigated and a remarkable development was seen. Perovskites drive interest because of their wide energy applications [1]. Perovskite materials with the general formula  $ABO_3$  (where  $A$  is an alkaline earth cation and  $B$  is the transition metal cation) are widely

studied by researchers for emerging energy applications [2]. Kumari et al. have synthesized pure  $BiFeO_3$  nanoparticles and reported their microstructural, magnetic, electric, and magnetocapacitance properties with good results.  $SrHfO_3$  perovskite material was synthesized by Zitouni et al. [3] and reported with a good bandgap. Many rare-earth-based perovskite materials were also widely studied by the researchers for their structural, morphological, optical, dielectric, magnetic, and electrical properties. Xukeer et al. reported the perovskite material  $YFe_{1-x}Mn_xO_3$  with enhanced gas sensing performance [4]. As a result, perovskite materials have gained interest because of their multiferroic, ferromagnetic, ferroelectric, dielectric, and magnetoelectric coupling properties [5]. Double perovskite structure derived from perovskite structure, with the general formula  $A_2B_2O_6$  (where  $A$  is an alkaline earth cation which coordinates with twelve oxygen anions and is larger in size and  $B$  is the transition metal cation which coordinates with six oxygen anions and is smaller in size). The double perovskite structure is

✉ T. Sharmili  
sharmiliaparna@gmail.com

<sup>1</sup> Research Centre of Physics, Fatima College (Autonomous),  
Affiliated to Madurai Kamaraj University, Madurai,  
Tamil Nadu, India

<sup>2</sup> Advanced Materials Laboratory, School of Physics, Madurai  
Kamaraj University, Madurai, Tamil Nadu, India

formed, when the A-site is partially substituted as  $A$  and  $A'$  ( $AA'B_2O_6$ ) or when the B-site is partially substituted as  $B$  and  $B'$  ( $A_2BB'O_6$ ). The presence of two rare-earth elements in A-site or the presence of two transition metal elements in B-site of a double perovskite material can provide greater flexibility and stability than a single perovskite material composed of one  $A$  cation and one  $B$  cation. These remarkable features of adjustable structural properties of double perovskite materials paved the way for obtaining perovskite oxides with better functional performances [6]. Also, the presence of defects tuned the material's properties into desirable effects. Oxide double perovskite nanostructures were competitive alternatives to low-cost functional materials with high efficiency and stability to replace the state of the art materials. Among the double perovskite materials,  $R_2NiMnO_6$  had turned out as an excellent material due to its multiferroic behavior, which contributes to memory and magnetic storage devices [7]. R.J.Booth et al. investigated the structural, magnetic, and dielectric properties of  $R_2NiMnO_6$  and got excellent results [8]. Macedo Filho et al. reported the spin coupling effect of  $Y_2NiMnO_6$  with the better results than other double perovskite materials [9]. Jie Su et al. showed the multiferroic behavior of  $Y_2NiMnO_6$  [10]. In this study, double perovskite  $Y_2NiMnO_6$  (YNMO) nanostructures were synthesized by a hydrothermal route. Hydrothermal synthesis is one of the most commonly used solution reaction-based methods for the preparation of nanomaterials. In hydrothermal synthesis, the formation of nanomaterials, including their shape and size, can be controlled by the variation in the temperature and pressure conditions. Hydrothermal synthesis can generate nanomaterials that are not stable at elevated temperatures. The compositions of nanomaterial to be synthesized can be well controlled in hydrothermal synthesis with less loss of materials [11]. In most cases, formulations to prepare double perovskites are complicated and need harsh reaction conditions like high temperatures, in most of the cases. Great efforts are dedicated to developing rationally engineered double perovskite materials by controlling morphologies through the preparation methods. Only few reports are available for double perovskite materials in energy storage applications. For further explorations, the prepared YNMO double perovskite material is investigated here with potential for next generation magnetic and electric energy storage applications. Impedance spectroscopy provides information about grain, grain boundary, and relaxation frequency. Dielectric characteristics of materials are considered to be highly influenced by the effect of grain and grain boundaries, and provides information about the complex electrical parameters such as impedance, dielectric, AC conductivity, and modulus [12]. Prepared YNMO nanostructures are investigated as cathode electrode for supercapacitor applications. The electrochemical performances of YNMO are explored by cyclic voltammetry curve with

change in concentration of the electrolyte at different scan rates. Impact of impedance, dielectric, and magnetic properties on the prepared YNMO is analyzed to improve their electrochemical energy storage properties.

## 2 Experimental procedure

As starting materials,  $Y(NO_3)_3 \cdot 6H_2O$ ,  $Ni(NO_3)_2 \cdot 6H_2O$ , and  $C_4H_6MnO_4 \cdot 4H_2O$  were dissolved in 40 ml of double distilled water and stirred for 15 min with a magnetic stirrer. The 5 M NaOH solution was added to the mixture under continuous stirring to adjust the pH and then stirred for 30 min until the solution turned brown. Then the mixture was transferred to a Teflon-lined autoclave and heated at 200 °C for 24 h. After it cools down to room temperature naturally, the obtained product was collected and washed several times with double distilled water, ethanol, and acetone in equal proportions. The washed sediments were then dried in an oven at 70 °C for 24 h. The resulting powder was calcined at 950 °C for 1 h in a furnace to get the double perovskite YNMO.

## 3 X-ray diffraction spectroscopy

To determine the phase and structure of YNMO, powder X-ray diffraction (PXRD) using  $CuK_\alpha$  radiation (PANalytical,  $\lambda = 1.5418 \text{ \AA}$ ) with  $2\theta$  ranging from 20° to 80° is directed at the synthesized sample. The pattern is shown in Fig. 1. The diffraction peaks in XRD pattern observed at Bragg's angles ( $2\theta$ ) 32.89°, 42.27°, 47.96°, 53.29°, 60.30° were indexed to a monoclinic structure with space group  $P21/n$  to diffraction planes (112), (202), (023), (131), (204). The obtained lattice parameters using X'pert Hi Score plus

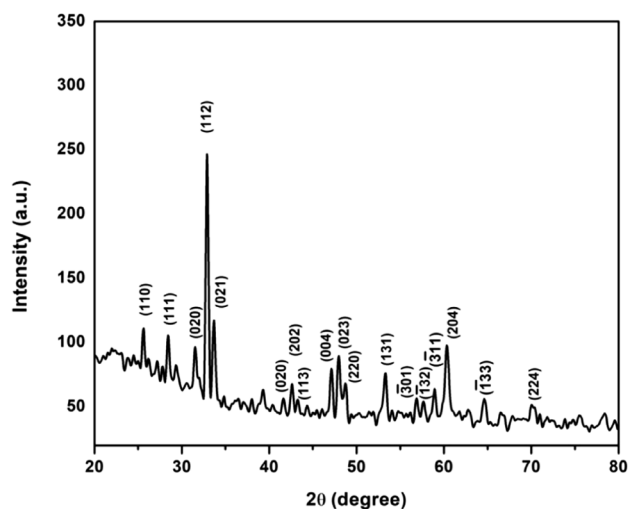
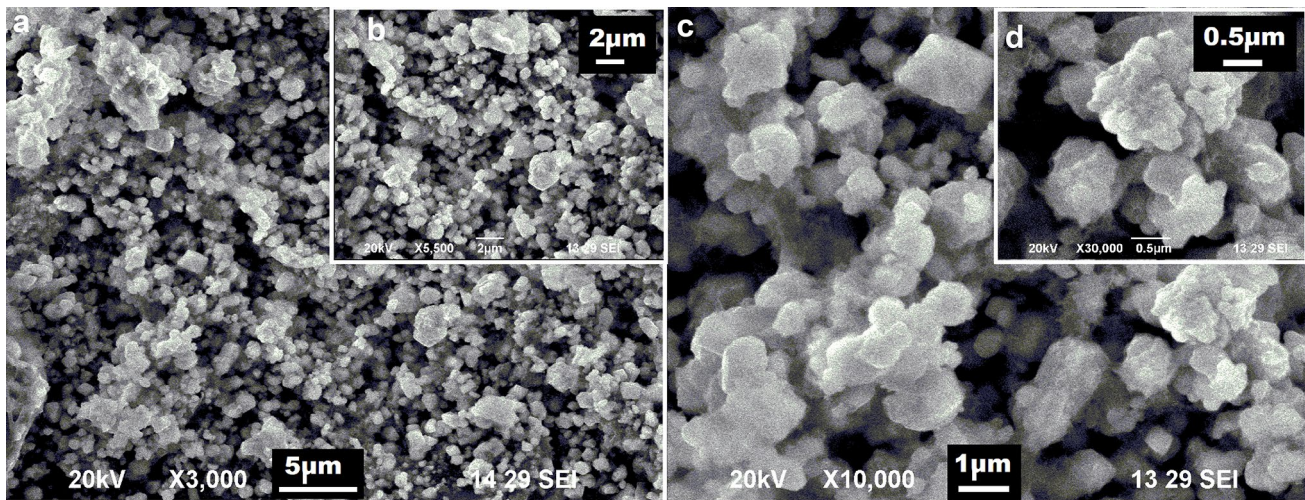


Fig. 1 X-ray diffraction pattern



**Fig. 2** SEM image of Y<sub>2</sub>NiMnO<sub>6</sub> at different magnifications

software were  $a = 5.338 \text{ \AA}$ ,  $b = 5.695 \text{ \AA}$ , and  $c = 7.696 \text{ \AA}$ , which are in good agreement with the reported results [13].

The tolerance factor  $t$  to determine the perovskite structure is calculated from,

$$t = 1/\sqrt{2}(r_Y + r_O) / \left( \frac{(r_{Ni} + r_{Mn})}{2} + r_O \right) \quad (1)$$

where  $r_Y$ ,  $r_{Ni}$ ,  $r_{Mn}$ , and  $r_O$  denote the ionic radii of yttrium, nickel, manganese, and oxide. It was reported that for  $t$  close to 1, a cubic perovskite structure is obtained. A tilt and rotation of the octahedral structure is obtained when the tolerance factor lies between  $1.00 \geq t \geq 0.97$  then structure becomes tetragonal and if  $t \leq 0.97$ , then structure becomes distorted and may undergo a monoclinic or orthorhombic structure [14]. Here, for the YNMO nanostructure, the calculated tolerance factor is less than 0.97. So, it is in good agreement with the monoclinic  $P21/n$  structure, which agrees with the reported results [13, 15]. Using the Scherrer equation, the calculated average value of crystalline size ( $D$ ) is 32.7 nm, dislocation density ( $\delta$ ) = 0.0108 nm<sup>-2</sup>, and microstrain ( $\xi$ ) = 3.557 lines/m<sup>2</sup>.

#### 4 Scanning electron microscopy with elemental analysis

Scanning electron microscopy is an important tool in studying structure, shape, and size of the prepared nanostructures. Figure 2 shows the SEM images of the prepared YNMO sample observed using the Jeol JSM 6390 Scanning Electron Microscope. This image shows the formation of irregular clusters of nanostructure with varying sizes, along with the formation of a few nanocubes. The elemental analysis of the

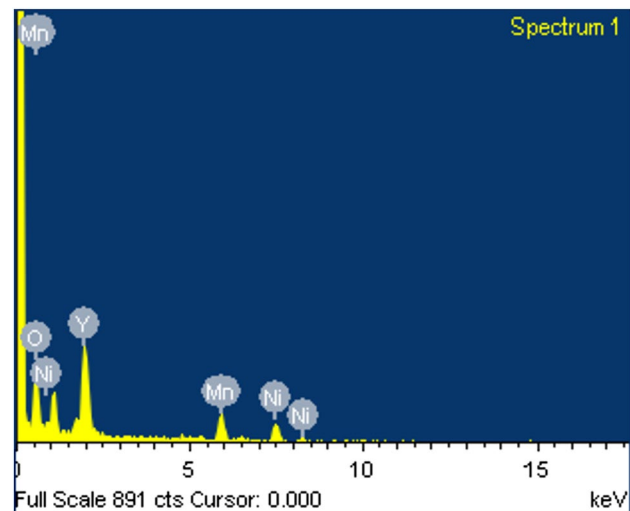


**Fig. 3** Elemental analysis of Y<sub>2</sub>NiMnO<sub>6</sub>

**Table 1** Elemental composition of Y<sub>2</sub>NiMnO<sub>6</sub>

Element	Weight %	Atomic %
Y	33.32	11.14
Ni	14.06	7.12
Mn	12.17	6.59
O	40.45	75.16

prepared sample was investigated by the EDAX technique (Fig. 3) and it confirms the presence of all the elements in appropriate proportion for the formation of double perovskite YNMO without any impurities. The weight percent and atomic percent of the elements present in the sample are shown in Table 1.



## 5 High-resolution transmission electron microscopy

Transmission electron microscopy is used to further investigate the morphology and microstructure of  $Y_2NiMnO_6$  nanoparticles. Figure 4a, b of the HRTEM analysis suggests that the higher and lower magnified  $Y_2NiMnO_6$  nanoparticles grow along the (111) crystallographic direction ( $c$  axis). The TEM image of a  $Y_2NiMnO_6$  nanoparticles (Fig. 4c) reveals a  $d$ -spacing of 0.56 nm. HRTEM of the corresponding selected area electron diffraction pattern may be attributed to the (311) plane for  $Y_2NiMnO_6$ . Fast Fourier transform (FFT) analysis (Fig. 4d) is performed on the lattice fringes and the diffraction spots are well indexed to the cubic spinel. The (111) and (311) oriented crystallographic peaks are well matching the existing XRD analysis.

## 6 Impedance study

Complex impedance spectroscopy (CIS) is a powerful technique to investigate the microstructural and electrical properties of a synthesized sample. The impedance measurement

is done on the sample to differentiate the grain, grain boundary, and electrode responses [16]. This complex impedance ( $Z$ ) has a real part ( $Z'$ ) and an imaginary part ( $Z''$ ) as,

$$Z = Z' + iZ'' \quad (2)$$

The real and imaginary parts of impedance are determined from the following Eqs. (3 and 4),

$$Z' = \left(\frac{Z}{d}\right) \cos \left[\varphi \left(\frac{3.14}{180}\right)\right] \quad (3)$$

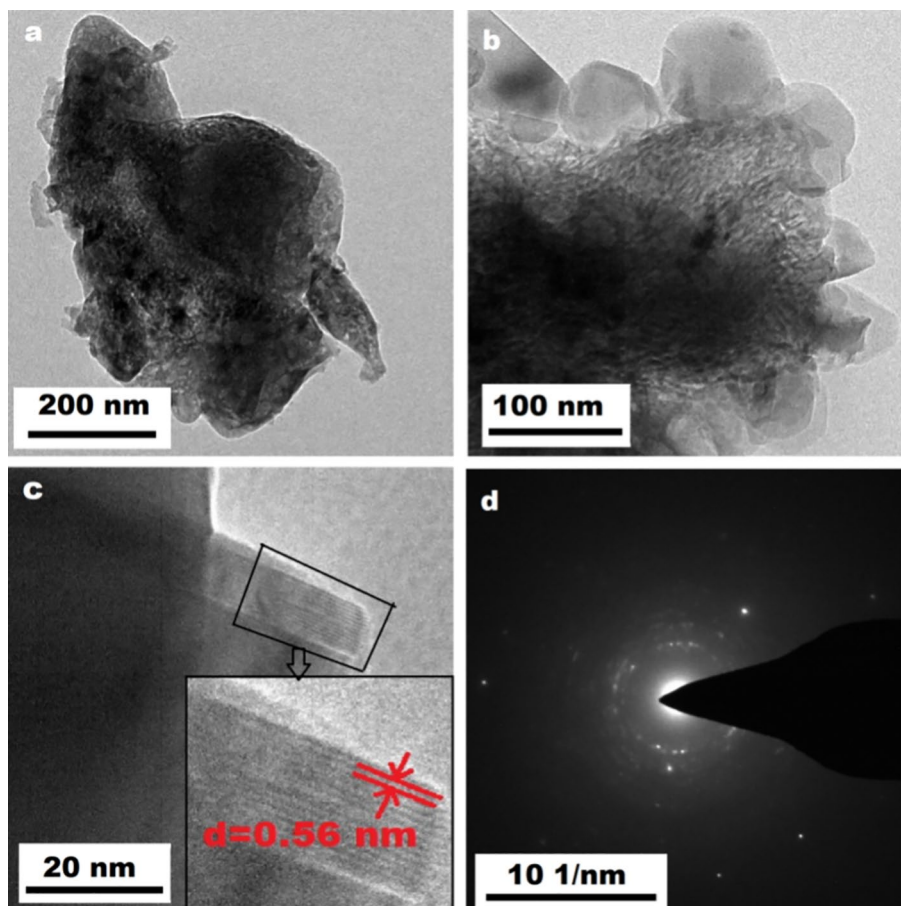
and

$$Z'' = \left(\frac{Z}{d}\right) \sin \left[\varphi \left(\frac{3.14}{180}\right)\right] \quad (4)$$

where  $Z$  is the complex impedance value (synthesized YNMO is pelletized and the values are taken from the HIOKI Hi Tester LCR Meter in the frequency range of 100 Hz–5 MHz),  $d$  (0.0016 m) is the thickness of the pellet, and  $\varphi$  is the phase angle.

In Fig. 5a  $Z'$  versus Frequency, it is found that the value of  $Z'$  (real part of impedance) decreases with the increase in frequency. The value of  $Z'$  decreases rapidly up to the frequency range of 1 MHz and above 1 MHz it is slowly

**Fig. 4** a, b High and lower magnified TEM image for  $Y_2NiMnO_6$  and randomly distributed particles in various sizes. c The calculated  $d$ -spacing images of  $Y_2NiMnO_6$ . d The corresponding selected area electron diffraction pattern



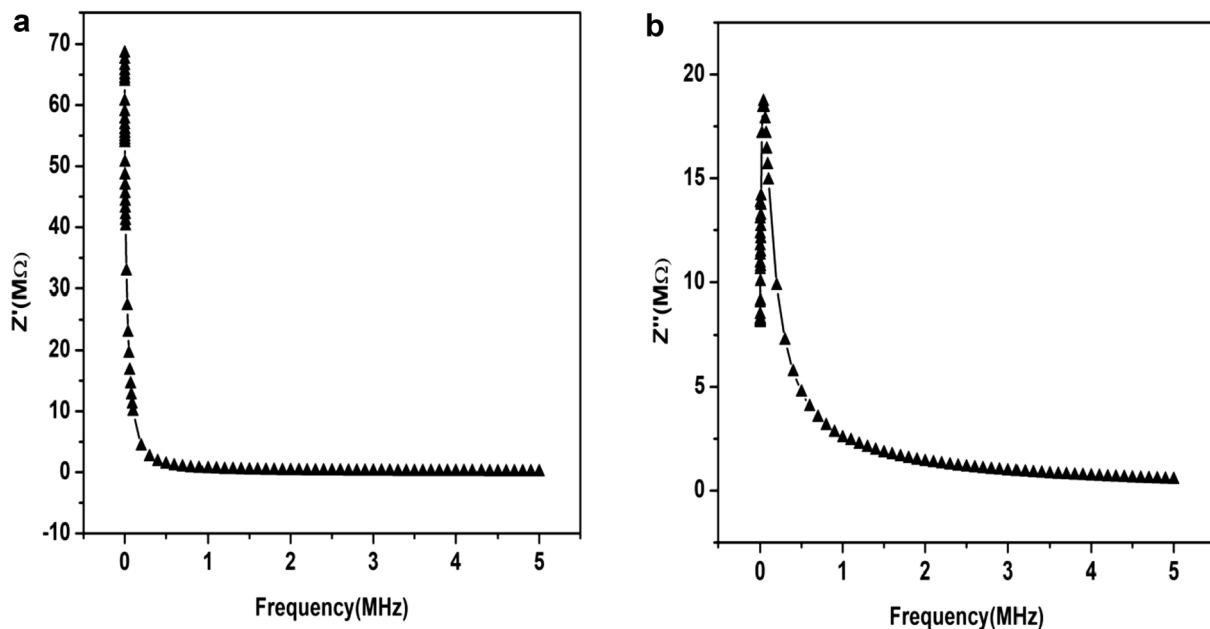


**Fig. 5** **a** Plot of real part of impedance ( $Z'$ ) versus frequency, **b** plot of imaginary part of impedance ( $Z''$ ) versus frequency

decreasing. It is observed that the value of  $Z'$  is frequency dependent. And it also shows the conductive nature of the material because the rise in AC conductivity with frequency corresponds to the electron hopping mechanism. As a result, as the frequency increases, the impedance decreases [17]. In case of  $Z''$  (imaginary part of impedance) versus frequency (Fig. 5b), at a particular frequency (below 0.5 MHz), the value of  $Z''$  attains the maximum. This indicates the presence of a relaxation or resonance peak in the material. Relaxation occurs due to the immobile charges or vacancies in the dielectric material and the main reason for the resonance peak is due to the matching of frequencies between the applied AC frequency and the hopping frequency of charge carriers [18]. The frequency at which  $Z''$  reaches its maximum value is called the relaxation frequency ( $f_r$ ). The inverse of  $f_r$  is known as relaxation time [19]. Between the frequency range of 0.5 and 5 MHz, the value of  $Z''$  slowly decreases and remains constant.

## 7 Nyquist plot

Figure 6 displays the Nyquist plot, which describes the variation of  $Z'$  with  $Z''$  at room temperature with respect to frequency. The semicircular nature of the low-, medium-, and high-frequency regions gives information about the effect of grain (bulk) and grain boundaries in the complex impedance plot by the separate semicircle curves [20]. According to the Debye relaxation type, the center of the semicircle coincides with the real impedance axis, that is  $Z'$ . Here in

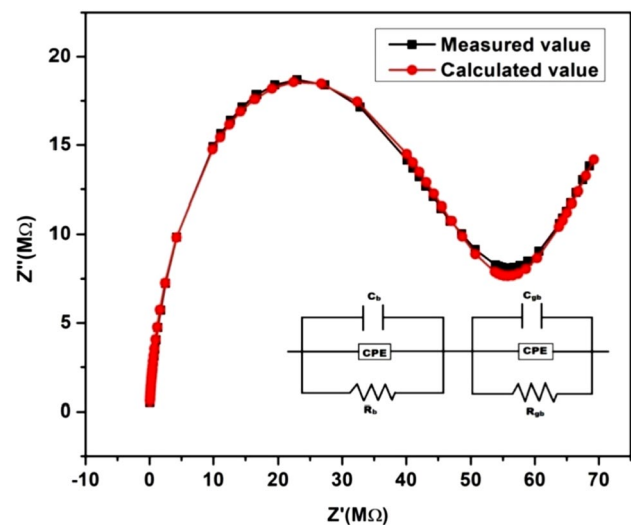


**Fig. 6** Nyquist plot for  $\text{Y}_2\text{NiMnO}_6$  and equivalent circuit (with fitting)

this plot, it is observed that the center of the semicircle does not coincide with the real impedance axis  $Z'$ . So, it falls into the non-Debye type of relaxation. This may be due to some imperfections in the sample during synthesis [21].

The semicircle in Fig. 6 indicates the effect of the grain boundary, and the curve next to the semicircle indicates the grain effect. ZSimp3.20 software is used to fit the semicircle with the theoretical one and to determine the equivalent circuit. The equivalent circuit is obtained by the series connection of parallel capacitances ( $C$ ) and resistances ( $R$ ). The

series arrangement of two CQR (Q-constant phase element, which is indicated as CPE in the circuit) is manifested by the Nyquist plot, which describes the effect of grain and grain boundary. The constant phase element (CPE) is introduced to the circuit to represent the deviation in the Debye-type relaxation (non-Debye type relaxation) [20]. As a result of this (Table 2), it is confirmed that the grain boundary is more resistive than the grain.

### 8 Dielectric study

The frequency variation (100 Hz–5 MHz) of the dielectric constant ( $K$ ) and dielectric loss ( $\tan\delta$ ) of the sample at room temperature was studied using the HIOKI Hi Tester LCR Meter to observe the dielectric performance of YNMO.

**Table 2** Fitted parameters for equivalent circuit in Nyquist plot

Parameters	Grain boundary	Grain
Resistance ( $\Omega$ )	$R_b = 5.138E11$	$R_{gb} = 5.337E7$
Capacitance ( $F$ )	$C_b = 2.047E-30$	$C_{gb} = 5.529E-14$
Constant phase element, CPE ( $S s^n$ )	$2.805E-9$	$1.392E-11$
Frequency power ( $n$ )	0.4976	0.532

Chi-squared = 0.0013 (error)

The dielectric constant ( $K$ ) signifies amount of energy that can be stored in the dielectric material. In the presence of an applied AC field, the electrical energy loss as heat during the polarization in the dielectric material is called dielectric loss ( $\tan\delta$ ) [16].

The dielectric constant and dielectric loss are determined using the formula,

$$K = C_p d / \epsilon_o A \tag{5}$$

$$\tan \delta = Z' / Z'' = K'' / K' = M'' / M' \tag{6}$$

where  $C_p$  is the parallel capacitance,  $d$  is the thickness of the pellet,  $\epsilon_o$  is the permittivity of free space, and  $A$  is the area of the pellet [22, 23].

From Fig. 7a, b, it is confirmed that the dielectric constant ( $K$ ) and dielectric loss ( $\tan\delta$ ) decrease with an increase in the frequency. The Maxwell–Wagner model explains the nature of frequency-dependent dielectric properties of the material. This model explains that the dielectric materials have poorly conducting grain boundaries and highly conducting grains, which is confirmed by the fitted CPE circuit’s Table 2. At lower frequencies, grain boundaries are more effective and at higher frequencies, the grains are more effective [21]. This is because of the hopping of electrons between Ni and Mn cations, which cannot go beyond the variation in frequency [24].

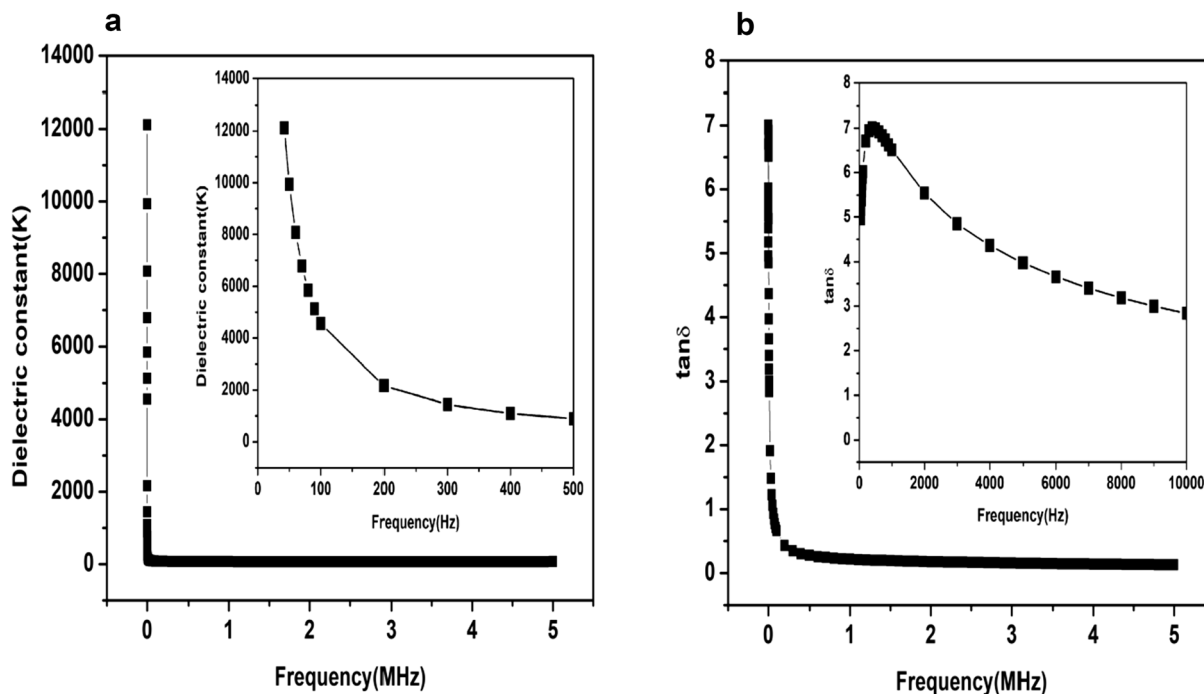


**Fig. 7** a, b Plot of dielectric constant ( $K$ ) and dielectric loss ( $\tan\delta$ ) with frequency in MHz (Inset of a, b plot of  $K$  and  $\tan\delta$  with frequency in Hz)

At high-frequency region, electrons are more active in grain, and at low-frequency regions, electrons are more active in grain boundaries during electrical conductivity. Therefore, grain boundaries have a more resistive nature than the grain itself. So both the values of  $K$  and  $\tan\delta$  are maximal in the low-frequency region because a large amount of energy is needed to transfer electrons. And, in the high-frequency region for both  $K$  and  $\tan\delta$ , minimum amount of energy is needed to transfer the charge carrier and for the alignment of dipoles [20]. The relaxation peak is present in the lower frequency region of the dielectric loss graph, which is known as the relaxation frequency ( $f_r$ ) and the inverse of  $f_r$  is called relaxation time [22]. This is because the electrons in dielectric materials take some time to rearrange themselves. It is noted that the dielectric loss also depends on the relaxation of the dielectric material.

The effects of temperature on dielectric constant ( $K$ ) and dielectric loss ( $\tan\delta$ ) are depicted in the plot of  $K$  and  $\tan\delta$  with frequency at different temperatures of the synthesized YNMO. From Fig. 8a, b it is noted that below 100 °C, the values of  $K$  and  $\tan\delta$  are independent of frequency and above 100 °C, the values of  $K$  and  $\tan\delta$  are dependent on frequency. The increase in  $K$  and  $\tan\delta$  values at higher temperatures may be due to the distribution of charge carriers, the generation of defects or an unknown impurity present in the prepared sample [25].

## 9 AC electrical conductivity

Electrical conductivity is the study of the physical properties of a material with the effect of an electric field. Electrical conductivity in dielectric materials is associated with the movement of free ions or charge under the applied electric field. Based on the types of ions (cations/anions) or charge carriers (electrons/holes), the electrical conductivity in the dielectric material is categorized as an ionic or electronic conductor [25].

From the obtained dielectric data, the formula for AC conductivity is given by [13],

$$\sigma_{AC} = \omega \epsilon_0 K \tan \delta \quad (7)$$

where  $\sigma_{AC}$  is AC conductivity,  $\omega$  is angular frequency, and  $\epsilon_0$  is permittivity in free space.

From Fig. 9, it is clear that the conductivity increases as frequency increases. At low frequencies, the conductivity is frequency independent. This is because of the random diffusion of charge carriers due to hopping. At higher frequencies, conductivity increases with an increase in frequency that is frequency dependent due to dispersion of charge carriers. To understand this mechanism, Jonscher power law is used [16, 26],

$$\sigma_i(\omega) = \sigma_{DC} + \sigma_1(\omega) = \sigma_{DC} + A\omega^n \quad (8)$$

where  $\sigma_i(\omega)$  is total conductivity,  $\sigma_{DC}$  is the DC conductivity term and it is frequency independent ( $f > 100$  kHz),  $\sigma_1(\omega) \propto \omega^n$  which gives rise to the conductivity at higher frequencies

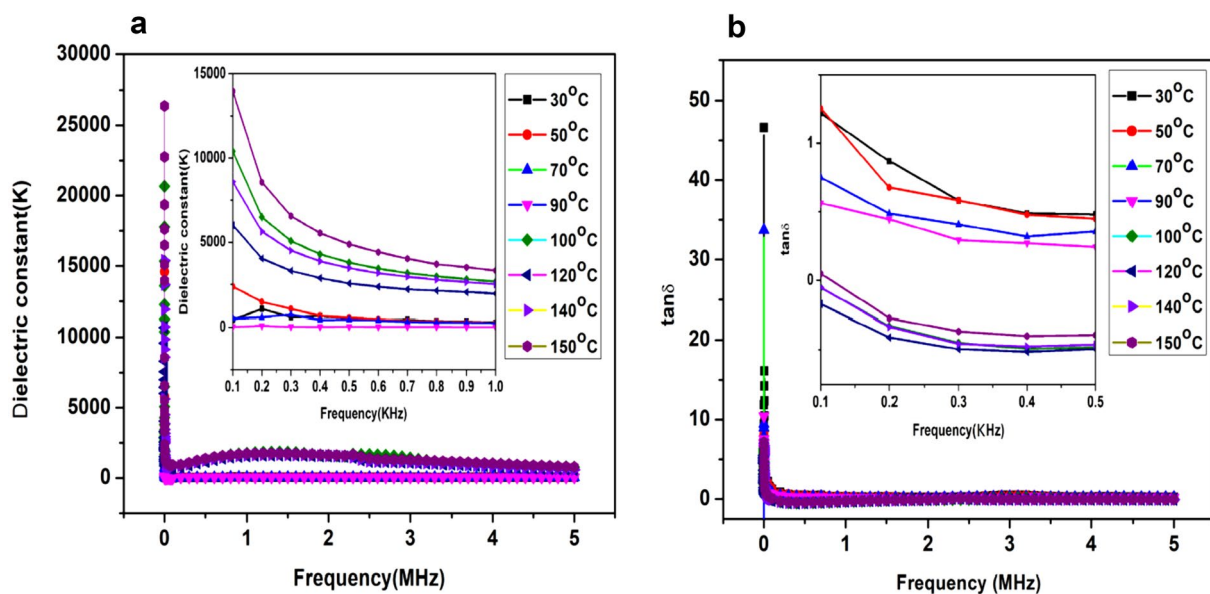


**Fig. 8** **a** Variation of dielectric constant ( $K$ ) and **b** dielectric loss ( $\tan\delta$ ) at different temperature with frequency in MHz (Inset of **a**, **b** variation of  $K$  and  $\tan\delta$  at different temperature with frequency in KHz)

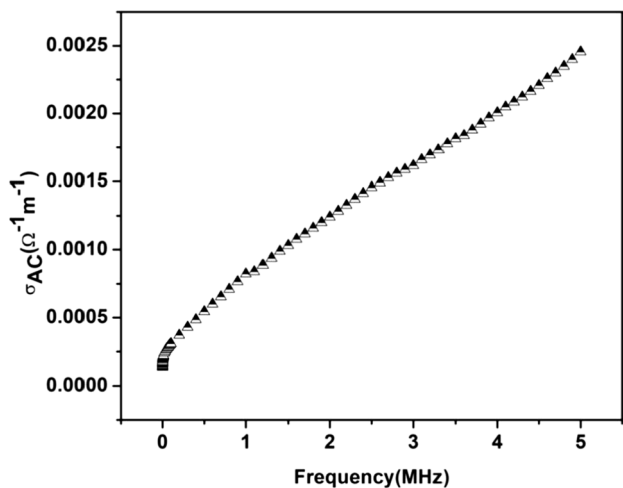


Fig. 9 Plot of AC conductivity ( $\sigma_{AC}$ ) versus frequency

and it is the reason for dispersion of the charge carrier,  $A$  is the strength of the polarizability, exponent term  $n$  can lie between  $0 < n < 1$ .

### 10 Electrical modulus analysis

The electrical modulus analysis is defined by the grain, grain effect, conductivity, and relaxation behavior [16]. The complex function of electrical modulus is,

$$M = M' + iM'' \tag{9}$$

The real part of electrical modulus ( $M'$ ) and the imaginary part of electrical modulus ( $M''$ ) can be determined from the formula [23],

$$M' = \omega C_0 Z'' \tag{10}$$

and

$$M'' = \omega C_0 Z' \tag{11}$$

where  $C_0 = \epsilon_0 A/d$  ( $\epsilon_0$  is permittivity in free space,  $A$  is the area of the pellet, and  $d$  is the thickness of the pellet).

In the  $M'$  plot (Fig. 10a), we noted that there is a gradual increase in  $M'$  with increase in frequency. The value of  $M'$  is nearly zero in the low-frequency region. This is due to the short-range mobility of charge carriers during the conduction process and the insufficient restoring force for the flow of charge carriers, so that the value of  $M'$  is very small.

In  $M''$  plot (Fig. 10b), we observed the presence of peak. It increases with a rise in frequency, attains maximum value at a particular frequency, and then suddenly decreases. This indicates the presence of relaxation in the dielectric material because of the hopping of electrons [20].

In Fig. 11, the variations in the imaginary parts of impedance  $Z''$  and  $M''$  as a function of frequency give information about the low capacitance and high resistance and it also differentiates between the relaxation peak which is due to short-range flow or long-range flow of charge carriers. If there is a mismatching of peaks between  $Z''$  and  $M''$ , it confirms the short-range flow, and a match of peaks confirms the long-range flow of charge carriers. From the studied sample, it is noted that the peaks are mismatched. So, it

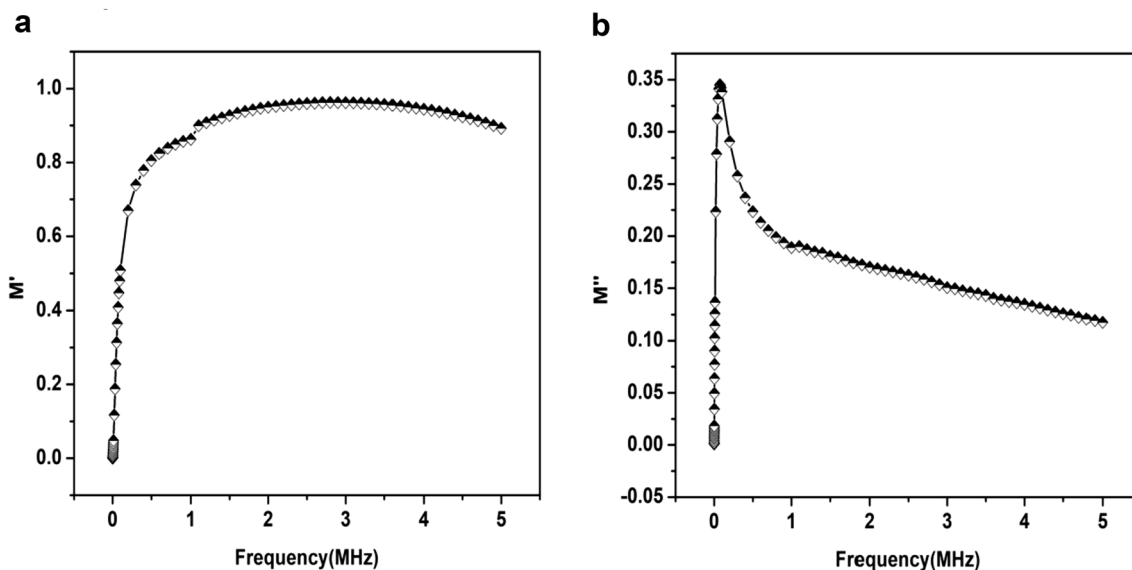


Fig. 10 a Plot of  $M'$  versus frequency and b plot of  $M''$  versus frequency



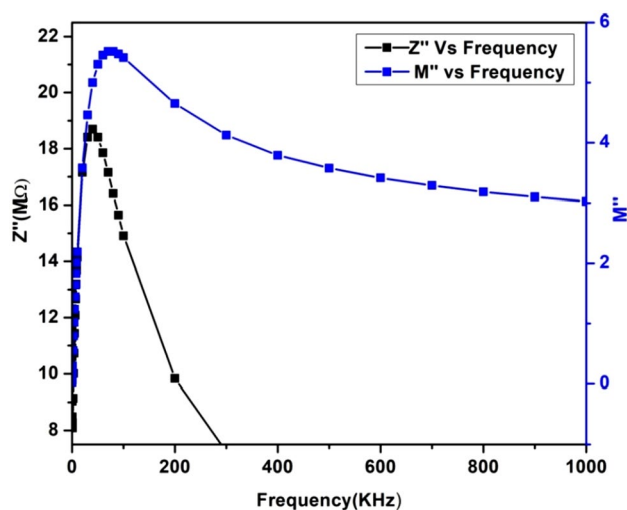


Fig. 11 Variation of  $Z''$  and  $M''$  with frequency

belongs to the short-range flow of charge carriers and the non-Debye relaxation type [20].

## 11 Electrochemical measurement

The cyclic voltammetry (CV) of synthesized YNMO nanostructures is analyzed using a BioLogic SP-50 electrochemical instrument at different scan rates using a three-electrode system. The three-electrode system was composed of a counter electrode (platinum rod), a reference electrode (Ag/AgCl), a working electrode and KOH as an electrolyte. The working electrode was fabricated by taking 85 wt% of active material (YNMO), 10 wt% carbon black, and 5 wt% polyvinylidene fluoride (PVDF) as a binder, mixed with N-methyl-2-pyrrolidinone (NMP) to get slurry formation and coating it evenly on the nickel foam substrate (geometrical working area is 1 cm<sup>2</sup>) and drying it for several hours [13].

The rectangular curve in the CV graph represents the electric double layer capacitor but in this CV graph, the appearance of redox peaks confirmed the presence of faradic redox reaction that manifests the pseudocapacitive behavior of the synthesized YNMO [20]. The reason for the peak is due to the faradic redox reaction of  $(B/B')-O/(B/B')-O-OH$  (where  $B = Ni$  and  $B' = Mn$ ), i.e.,  $(Ni^{2+}/Ni^{3+})$ ,  $(Mn^{2+}/Mn^{3+})$ , and  $(Mn^{3+}/Mn^{4+})$  ions with OH as a supporting ion in YNMO.

The effect of electrolyte on cathodic and anodic peaks can be observed in CV (Fig. 12a–c) by changing the concentration of KOH solution (0.5 M, 1 M, and 2 M) at different scan rates. For all three (0.5 M, 1 M, and 2 M) solutions of KOH, there is a shift in cathodic and anodic peaks toward lower potentials, indicating the lower charge/discharge potential of electrode in increasing concentration of KOH solution

[27]. And also, the faradic redox process is controlled with the enhancement of scan rates due to the development of overpotential. It is observed that the highest point of the anodic peak increases with an increase in scan rates. This is because the formation of a diffusion layer on the electrode surface is thick due to the longer time span at lower scan rates. For higher scan rates, the formation of the diffusion layer is thin due to the shorter time span. Therefore, faradic redox reaction is a rate-controlled process; that is, at lower scan rates, bulk OH<sup>−</sup> ions diffusion dominates and surface effect dominates at higher scan rates due to the formation of a thin diffusion layer on the electrode surface [28, 29].

From the CV graph, specific capacitance ( $C_p$ ) can be calculated using the following equation,

$$C_p = A/(mv\Delta V) \quad (12)$$

where  $A$  denotes the integral area enclosed by the CV curve,  $m$  is the mass coated on the nickel foam,  $v$  is scan rate, and  $\Delta V$  is the potential window. The specific capacitance ( $C_p$ ) calculated from the CV curves are tabulated (Table 3).

The calculated values of  $C_p$  and scan rates are plotted in Fig. 12d–f. And it confirmed that the value of  $C_p$  decreases with an increase in scan rate. This shows that the active material contribution is greater in lower scan rates and this behavior is also due to the bulk OH<sup>−</sup> ions diffusion as mentioned above [27] (Table 4).

It is noted that a maximum specific capacitance of 78.6 F/g was measured for the synthesized YNMO nanostructures when 2 M KOH was used as the electrolyte, which is slightly higher than any reported value of specific capacitance for the same material [13]. This suggests that the YNMO nanostructure could be useful in energy storage like supercapacitors.

## 12 Magnetic properties

Figure 13 shows the M–H loop of the YNMO nanostructure. The room-temperature hysteresis loop exhibits paramagnetism with a very small coercive field and remnant magnetization. Due to the larger surface area of nanostructures, overall magnetization is reduced. It should also be noted that loops barely close and do not truly saturate, even at high fields. This has been reported for epitaxial LCMO thin films as evidence of spin glass-like behavior as observed for LCMO ceramics synthesized by standard solid-state reactions [31]. The jog in magnetization at zero field was also observed in YNMO as depicted in Fig. 13 [31]. It should be noted that YNMO exhibits a bi-loop feature, as shown in the inset of Fig. 13 and this bi-loop is reported in Ca<sub>2</sub>FeReO<sub>6</sub> double perovskites as well. [32]. However, evidence of second magnetic phase in YNMO is not observed and the bi-loop magnetization jump near zero field is due

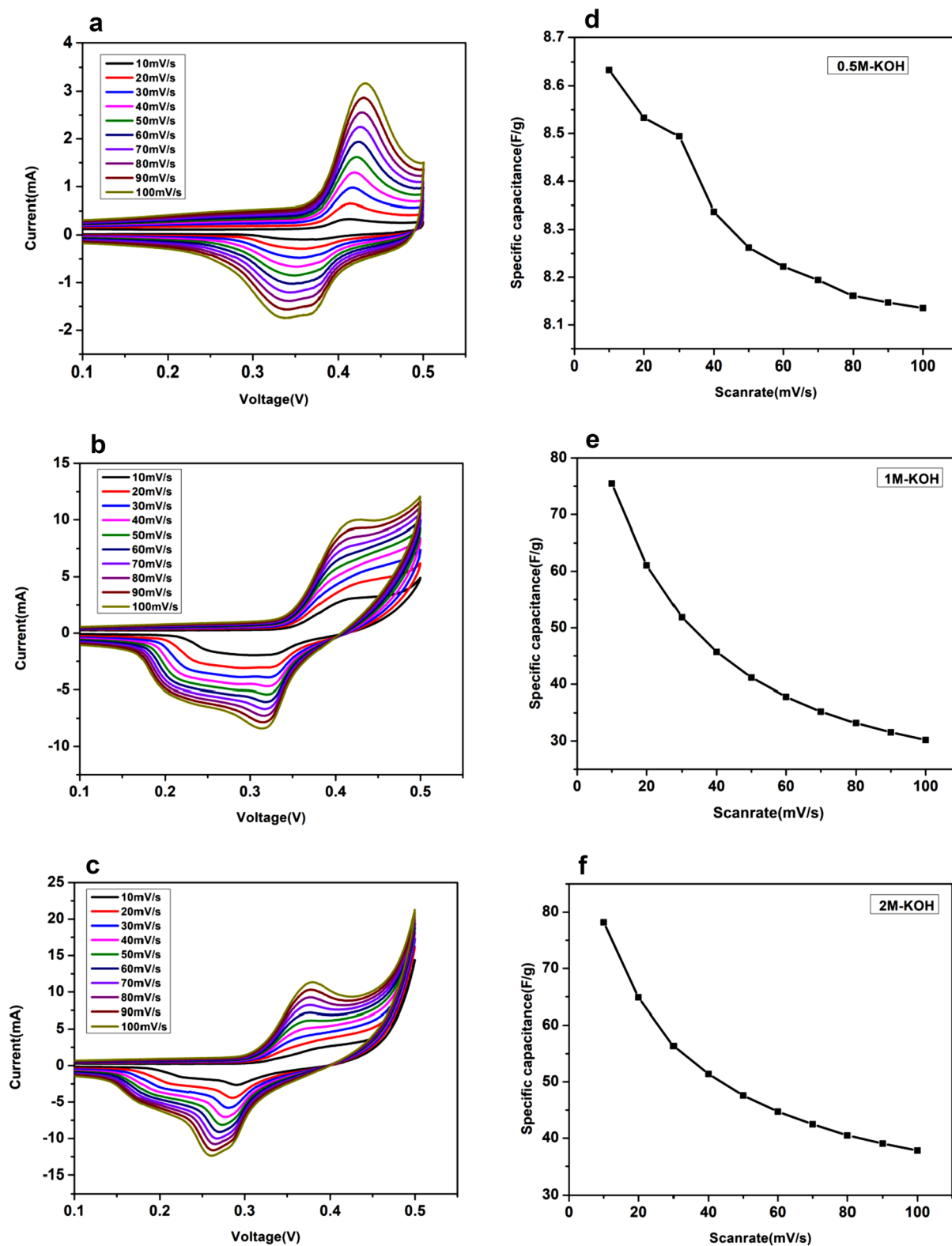


**Fig. 12** a–c Cyclic voltammogram of  $Y_2NiMnO_6$  in 0.5 M solution of KOH, 1 M solution of KOH, and 2 M solution of KOH. d–f Plot of specific capacitance versus scan rate for 0.5 M KOH, 1 M KOH, and 2 M KOH

**Table 3** Calculated specific capacitance values

Scan rates (mV/S)	Specific capacitance, $C_p$ (F/g)		
	0.5 M-KOH	1 M-KOH	2 M-KOH
10	8.633	75.476	78.201
20	8.533	61.042	64.869
30	8.494	51.863	56.330
40	8.337	45.684	51.373
50	8.262	41.168	47.568
60	8.222	37.823	44.707
70	8.194	35.212	42.467
80	8.161	33.187	40.485
90	8.147	31.556	39.042
100	8.135	30.201	37.815

to the presence of multiple magnetic domains with different coercivity as discussed in the reported results [33]. The saturation moment is much smaller and known anti-site defects [32]. It cannot be ruled out that these nanostructures exhibit some fraction of surface plasmon resonance sites, some disorder, and/or large fractions of anti-site disorder that result in low-specific saturation magnetization. This

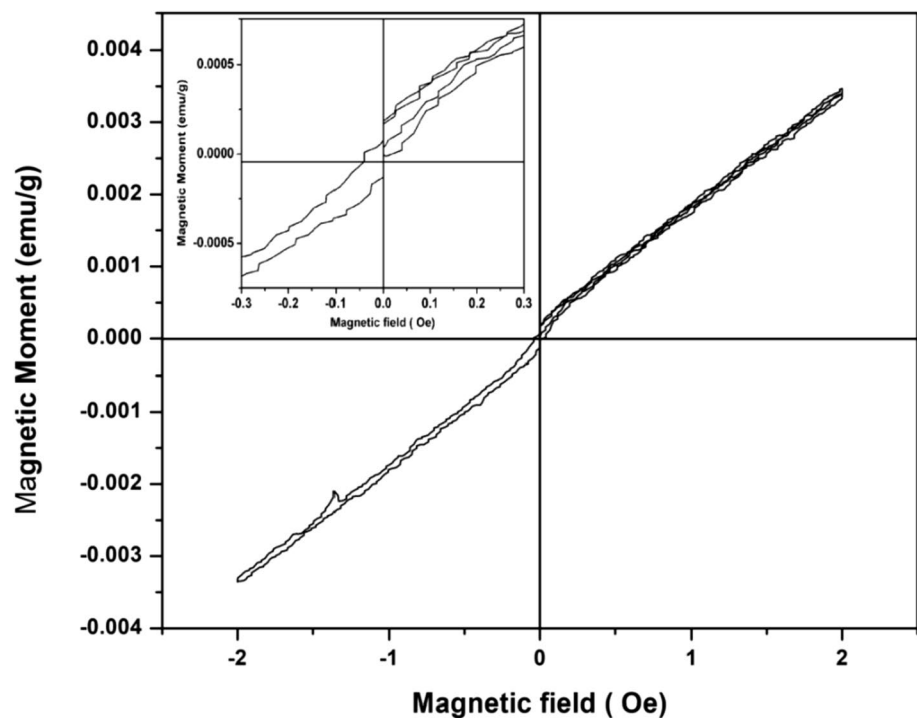
may be due to the magnetic impurity [34]. This may arise from the existence of oxygen deficiency, which promotes the appearance of oxygen vacancies,  $\text{Mn}^{3+}/\text{Mn}^{4+}$  mixed valence state, and anti-site disorder of  $\text{Mn}^{4+}$  and  $\text{Ni}^{2+}$  in the samples. Besides, the anti-site defects have a remarkable influence on the magnetic properties of double perovskites, since the  $\text{Mn}^{4+}-\text{O}-\text{Mn}^{4+}$  and  $\text{Ni}^{2+}-\text{O}-\text{Ni}^{2+}$  exchange interactions are weak ferromagnetic [35], which prevent the complete saturation of magnetization. Specifically, anti-site disorder leads to antiferromagnetic couplings, while the predominant  $\text{Mn}^{4+}-\text{O}^{2-}-\text{Mn}^{4+}$  of the ordered structure is paramagnetic [33]. This result coincides with the reported results [15, 36]. The hysteresis loop appeared at 2 Oe, with remnant magnetization ( $M_r$ ) at  $2.017\text{E}-4$  emu/g and coercive field ( $H_c$ ) at  $3.836\text{E}-2$  Oe.

### 13 Conclusion

In summary, the YNMO nanostructures are synthesized via hydrothermal method. The powder X-ray diffraction confirms the formation of a monoclinic structure with a  $P21/n$  space group and a particle size of 32.7 nm. The scanning

**Table 4** Comparison table of specific capacitance value with other work

S. no.	Composition	Synthesis/morphology	$C_p$ (F/g)	References
1.	$\text{Y}_2\text{NiMnO}_6$	Hydrothermal/nanowires	77.76	[13]
2.	$\text{Dy}_2\text{NiMnO}_6$	Hydrothermal/mesoporous spheres	395.2	[30]
3.	$\text{Y}_2\text{NiMnO}_6$	Hydrothermal/nanostructure	78.6	Present work

**Fig. 13** Room-temperature M-H loop of  $\text{Y}_2\text{NiMnO}_6$  nanostructures (Inset of this figure M-H loop of  $\text{Y}_2\text{NiMnO}_6$  at lower scale)

electron microscope reveals the formation of the YNMO nanostructure. EDAX spectra confirm the presence of Y, Ni, Mn, and O without any other impurities. The impedance, modulus, and dielectric studies of the prepared YNMO were analyzed with a change in frequency. Impedance and dielectric studies confirmed the presence of relaxation frequency of non-Debye relaxation type that arises due to the hopping of electrons. Nyquist plot revealed electrical behavior with the effect of grain and grain boundary. AC electrical conductivity study showed the frequency-dependent curve with an increase in conductivity and an increase in frequency because of the dispersion of the charge carriers. Room-temperature magnetic characterization revealed paramagnetic behavior of YNMO at room temperature. The electrochemical analysis of synthesized YNMO confirmed pseudocapacitive nature with enhanced specific capacitance with an increase in concentration of KOH, 8.633 F/g for a 0.5 M solution of KOH, 75.476 F/g for a 1 M solution of KOH, and 78.201 F/g for a 2 M solution of KOH. Further detailed studies at various temperatures are needed for a better understanding of the nature of the magnetic state and the dynamic characteristics observed here for YNMO nanostructures. The increased value of specific capacitance enables the YNMO nanostructures, a potential candidate for energy storage applications.

**Data availability statement** Datas pertaining towards characterisations are already included in the manuscript. Further datas shall be provided on request due to privacy.

## References

1. A. Kostopoulou, E. Kymakis, E. Stratakis, Perovskite nanostructures for photovoltaic and energy storage devices. *J. Mater. Chem.* (2018). <https://doi.org/10.1039/C8TA01964A>
2. N. Wang, X. Luo, L. Han, Z. Zhang, R. Zhang, H. Olin; Y. Yang, Structure, performance, and application of BiFeO<sub>3</sub> nanomaterials. *Nanomicro Lett.* **12**(1), 81 (2020). <https://doi.org/10.1007/s40820-020-00420-6>
3. H. Zitouni, N. Tahiri, O. El Bounagui et al., Physical properties of perovskite SrHfO<sub>3</sub> compound doped with S for photovoltaic applications: the ab initio study. *Appl. Phys. A* **126**, 800 (2020). <https://doi.org/10.1007/s00339-020-03987-4>
4. A. Xukeer, Wu, Zhaofeng, Q. Sun, F. Zhong, M. Zhang, M. Long, H. Duan, Enhanced gas sensing performance of Perovskite YFe<sub>1-x</sub>Mn<sub>x</sub>O<sub>3</sub> by doping manganese ions. *RSC Adv.* **10**(51), 30428–30438 (2020). <https://doi.org/10.1039/d0ra01375g>
5. A.J. Preethi, M. Ragam, Effect of doping in multiferroic BFO: a review. *J. Adv. Dielect.* **11**(6), 2130001 (2021). <https://doi.org/10.1142/S2010135X21300012>
6. J. Singh, A. Kumar, A. Kumar, Facile solvothermal synthesis of nano-assembled mesoporous rods of cobalt free—La<sub>2</sub>NiFeO<sub>6</sub> for electrochemical behaviour. *Mater. Sci. Eng. B* **261**, 114664 (2020). <https://doi.org/10.1016/j.mseb.2020.114664>
7. T. Jia, Z. Zeng, H.Q. Lin, The collinear↑↑↓ magnetism driven ferroelectricity in double-Perovskite multiferroics. *J. Phys. Conf. Ser.* **827**(1), 012005 (2017). <https://doi.org/10.1088/1742-6596/827/1/012005>
8. R.J. Booth, Fillman R., Whitaker H., A. Nag, R.M. Tiwari, K.V. Ramanujachary, J. Gopalakrishnan, S.E. Lofland, An investigation of structural, magnetic and dielectric properties of R<sub>2</sub>NiMnO<sub>6</sub> (R = rare earth, Y). *Mater. Res. Bull.* **44**(7), 1559–1564 (2009). <https://doi.org/10.1016/j.materresbull.2009.02.003>
9. M. Filho, R. Bezerra, A.P. Ayala, C.W. de Araujo Paschoal, Spin-phonon coupling in Y<sub>2</sub>NiMnO<sub>6</sub> double perovskite probed by Raman spectroscopy. *Appl. Phys. Lett.* **102**(19), 192902 (2013)
10. J. Su, Z.Z. Yang, X.M. Lu, J.T. Zhang, L. Gu, C.J. Lu, Q.C. Li, J.-M. Liu, J.S. Zhu, Magnetism-driven ferroelectricity in double perovskite Y<sub>2</sub>NiMnO<sub>6</sub>. *ACS Appl. Mater. Interfaces* **7**(24), 13260–13265 (2015). <https://doi.org/10.1021/acsami.5b00911>
11. Y.X. Gan, A.H. Jayatissa, Z. Yu, X. Chen, M. Li, Hydrothermal synthesis of nanomaterials. *J. Nanomat.* **2020**, 1 (2020)
12. R. Datta, S.K. Pradhan, S. Chatterjee, S. Majumdar, S.K. De, Dielectric and impedance spectroscopy of Sm<sub>2</sub>CoIrO<sub>6</sub> double perovskite. *J. Alloys Compd.* **876**, 160158 (2021). <https://doi.org/10.1016/j.jallcom.2021.160158>
13. M. Alam, K. Karmakar, M. Pal, K. Mandal, Electrochemical supercapacitor based on double perovskite Y<sub>2</sub>NiMnO<sub>6</sub> nanowires. *RSC Adv* **6**(115), 114722–114726 (2016). <https://doi.org/10.1039/C6RA23318J>
14. J.B. Philipp, P. Majewski, L. Alff, A. Erb, R. Gross, T. Graf, M.S. Brandt et al., Structural and doping effects in the half-metallic double perovskite A<sub>2</sub>CrWO<sub>6</sub> (A= Sr, Ba, and Ca). *Phys. Rev. B* **68**(14), 144431 (2003). <https://doi.org/10.1103/PhysRevB.68.144431>
15. R.P. Maiti, S. Dutta, M. Mukherjee, M.K. Mitra, D. Chakravorty, Magnetic and dielectric properties of sol–gel derived nanoparticles of double perovskite Y<sub>2</sub>NiMnO<sub>6</sub>. *J. Appl. Phys.* **112**(4), 044311 (2012). <https://doi.org/10.1063/1.4748058>
16. R. Das, R.N.P. Choudhary, Dielectric relaxation and magneto-electric characteristics of lead-free double perovskite: Sm<sub>2</sub>NiMnO<sub>6</sub>. *J. Adv. Ceram.* **8**(2), 174–185 (2019). <https://doi.org/10.1007/s40145-018-0303-3>
17. N. Ahmad, S. Khan, M.M.N. Ansari, Exploration of Raman spectroscopy, dielectric and magnetic properties of (Mn, Co) co-doped SnO<sub>2</sub> nanoparticles. *Physica B* **558**, 131–141 (2019). <https://doi.org/10.1016/j.physb.2019.01.044>
18. N. Ahmad, S. Khan, M. Mohsin, N. Ansari, Optical, dielectric and magnetic properties of Mn doped SnO<sub>2</sub> diluted magnetic semiconductors. *Ceram. Int.* **44**, 15972–15980 (2018). <https://doi.org/10.1016/j.ceramint.2018.06.024>
19. N. Panda, B.N. Parida, R. Padhee, R.N.P. Choudhary, Structural, dielectric and electrical properties of the Ba<sub>2</sub>BiNbO<sub>6</sub> double perovskite. *J. Mater. Sci. Mater. Electron.* **26**(6), 3797–3804 (2015). <https://doi.org/10.1007/s10854-015-2905-7>
20. R. Das, R.N.P. Choudhary, Studies of structural, dielectric relaxor and electrical characteristics of lead-free double perovskite: Gd<sub>2</sub>NiMnO<sub>6</sub>. *Solid State Sci.* **87**, 1–8 (2019). <https://doi.org/10.1016/j.solidstatesciences.2018.10.020>
21. P. Achary, S.K. Dehury, R.N.P. Choudhary, Structural, electrical and dielectric properties of double perovskites: BiHoZnZrO<sub>6</sub> and BiHoCuTiO<sub>6</sub>. *J. Mater. Sci. Mater. Electron.* **29**(8), 6805–6816 (2018)
22. M. Amin, H.M. Rafique, G.M. Mustafa, A. Mahmood, S.M. Ramay, S. Atiq, S.M. Ali, Effect of La/Cr co-doping on dielectric dispersion of phase pure BiFeO<sub>3</sub> nanoparticles for high frequency applications. *J. Mater. Res. Technol.* **13**, 1534–1545 (2021). <https://doi.org/10.1016/j.jmrt.2021.05.066>
23. A. Priyanka, K. Jha, Electrical characterization of zirconium substituted barium titanate using complex impedance spectroscopy. *Bull. Mater. Sci.* **36**(1), 135–141 (2013). <https://doi.org/10.1007/s12034-013-0420-0>



24. W.Z. Yang, X.Q. Liu, H.J. Zhao, Y.Q. Lin, X.M. Chen, Structure, magnetic, and dielectric characteristics of  $\text{Ln}_2\text{NiMnO}_6$  (Ln = Nd and Sm) ceramics. *J. Appl. Phys.* **112**(6), 064104 (2012). <https://doi.org/10.1063/1.4752262>
25. S. Hajra, S. Sahoo, R. Das, R.N.P. Choudhary, Structural, dielectric and impedance characteristics of  $(\text{Bi}_{0.5}\text{Na}_{0.5})\text{TiO}_3\text{-BaTiO}_3$  electronic system. *J. Alloys Compd* **750**, 507–514 (2018)
26. D.K. Mahato, A. Dutta, T.P. Sinha, Dielectric relaxation and ac conductivity of double perovskite oxide  $\text{Ho}_2\text{ZnZrO}_6$ . *Phys. B Condens. Matter* **406**(13), 2703–2708 (2011). <https://doi.org/10.1016/j.physb.2011.04.012>
27. M. Li, F. Liu, X. Zhang, J.P. Cheng, Comparative study of Ni–Mn layered double hydroxide/carbon composites with different morphologies for supercapacitor. *Phys. Chem. Chem. Phys.* (2016). <https://doi.org/10.1039/c6cp05119g>
28. J. Singh, A. Kumar, Solvothermal synthesis dependent structural, morphological and electrochemical behaviour of mesoporous nanorods of  $\text{Sm}_2\text{NiMnO}_6$ . *Ceram. Int.* **46**(8), 11041–11048 (2020)
29. J. Singh, A. Kumar, A. Kumar, Facile wet chemical synthesis and electrochemical performance of double perovskite- $\text{La}_2\text{NiMnO}_6$  for energy storage application. *Mater. Today Proc.* **48**, 587–589 (2022). <https://doi.org/10.1016/j.matpr.2021.05.231>
30. J. Singh, I. Rogge, U.K. Goutam, A. Kumar, Mesoporous spheres of  $\text{Dy}_2\text{NiMnO}_6$  synthesized via hydrothermal route for structural, morphological, and electrochemical investigation. *Ionics* **26**(10), 5143–5153 (2020)
31. H.Z. Guo, A. Gupta, T.G. Calvarese, M.A. Subramanian, Structural and magnetic properties of epitaxial thin films of the ordered double perovskite  $\text{La}_2\text{CoMnO}_6$ . *Appl. Phys. Lett.* **89**(26), 262503 (2006). <https://doi.org/10.1063/1.2422878>
32. E. Granado, Q. Huang, J.W. Lynn, J. Gopalakrishnan, R.L. Greene, K. Ramesha, Spin-orbital ordering and mesoscopic phase separation in the double perovskite  $\text{Ca}_2\text{FeReO}_6$ . *Phys. Rev. B* **66**(6), 064409 (2002)
33. M.P. Singh, S. Charpentier, K.D. Truong, P. Fournier, Evidence of bidomain structure in double-perovskite  $\text{La}_2\text{CoMnO}_6$  thin films. *Appl. Phys. Lett.* **90**(21), 211915 (2007). <https://doi.org/10.1063/1.2743387>
34. F. de Azevedo, B. João, R.F. Souza, J.C.A. Queiroz, T.H.C. Costa, C.P.S. Sena, S.G.C. Fonseca, A.O. da Silva, J.B.L. Oliveira, Theoretical and experimental investigation of the structural and magnetic properties of  $\text{La}_2\text{NiMnO}_6$ . *J. Magn. Magn. Mater.* **527**, 167770 (2021). <https://doi.org/10.1016/j.jmmm.2021.167770>
35. H. Nhalil, H.S. Nair, C.M.N. Kumar, A.M. Strydom, S. Elizabeth, Ferromagnetism and the effect of free charge carriers on electric polarization in the double perovskite  $\text{Y}_2\text{NiMnO}_6$ . *Phys. Rev. B* **92**(21), 214426 (2015). <https://doi.org/10.1103/PhysRevB.92.214426>
36. A. Kaippamagalath, J.P. Palakkal, A.P. Paulose, M.R. Varma, Structural and magnetic properties of multiferroic  $\text{Y}_2\text{NiMnO}_6$  double perovskite. *Ferroelectrics* **518**(1), 223–231 (2017). <https://doi.org/10.1080/00150193.2017.1360679>

**Publisher's Note** Springer Nature remains neutral with regard to jurisdictional claims in published maps and institutional affiliations.

Springer Nature or its licensor (e.g. a society or other partner) holds exclusive rights to this article under a publishing agreement with the author(s) or other rightsholder(s); author self-archiving of the accepted manuscript version of this article is solely governed by the terms of such publishing agreement and applicable law.